Supplementary Information (SI) for Nanoscale Advances.

Supplementary Information (SI)

Polymer/AgPt Bimetallic Nanoparticles Synergy: Optimizing Plasmonic Durability through Controlled Synthesis and Matrix Integration

Abeer Fahes, *[a] Lavinia Balan, [b] Caroline Andreazza-Vignolle, [a] Claudia de Melo, [a] Didier Zanghi [b] and Pascal Andreazza *[a]

---

[a] *ICMN, Université d'Orléans, CNRS ; 1b rue de la ferollerie, F-45071 Orléans, France*
[b] *CEMTHI, Université d'Orléans, CNRS ; 1 Av. de la Recherche Scientifique, Orléans, France*
* Correspondence: abeer.fahes@cnrs-orleans.fr; pascal.andreazza@univ-orleans.fr

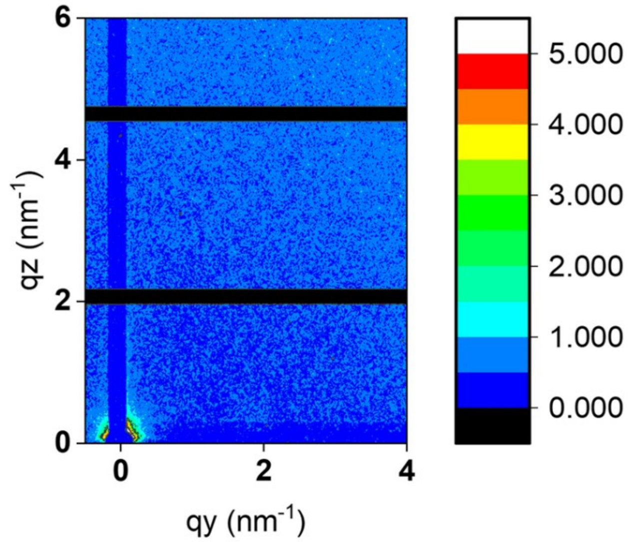

Figure S1: GISAXS 2D pattern on bare polymer film without nanoparticles.

GISAXS measurements of the bare polymer film **(Figure S1)** revealed no detectable scattering signal, confirming the polymer's non-porous nature, as porosity would otherwise produce measurable nanoscale density variations. In GISAXS, scattering typically originates from nanoscale density variations (e.g., pores, particles, or structural inhomogeneities).

Also, this dense microstructure arises from the rapid UV-initiated polymerization of a solvent-free acrylate formulation composed solely of monomer and photoinitiator. The absence of solvents or porogens in the formulation suppresses phase separation during curing, thereby inhibiting pore formation [1,2]. In contrast, conventional porous polymer systems typically rely on phase-separating additives—such as solvent/non-solvent mixtures—and carefully controlled solvent evaporation to induce porosity through self-assembly or templating mechanisms. The lack of such components and processes in our system is consistent with the formation of a non-porous polymer network.

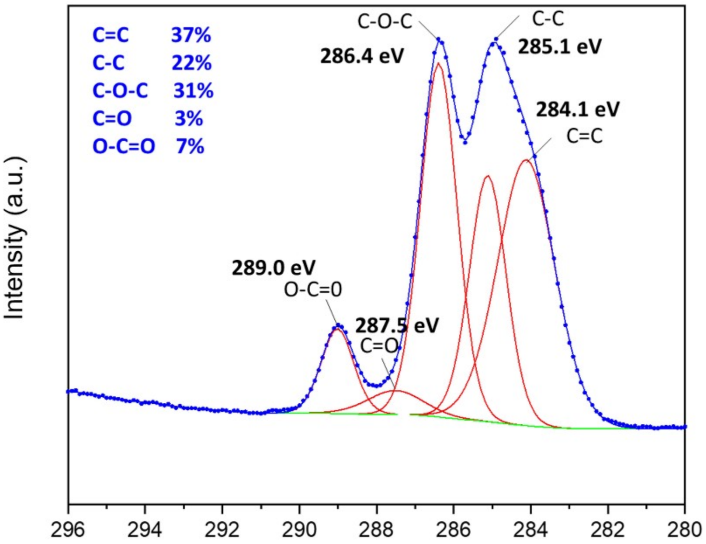

Figure S2: Deconvoluted XPS C1s core-level spectrum of the monomer.

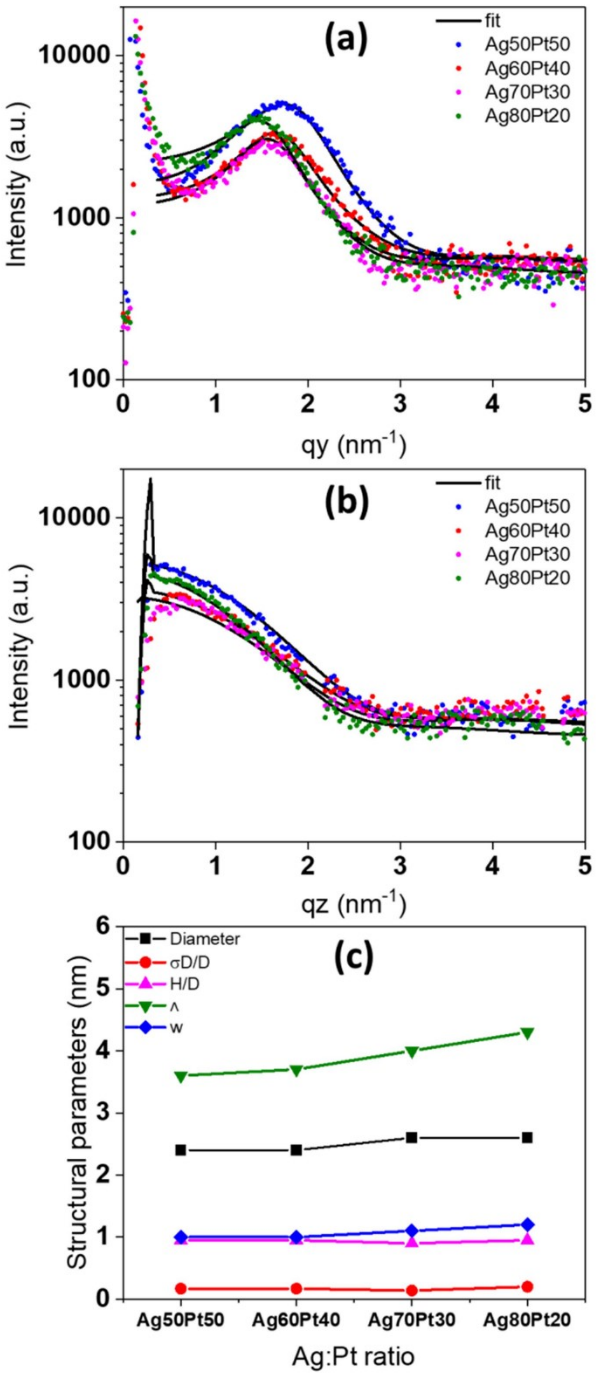

Figure S3: GISAXS structural analysis of Si/polymer/AgPt bimetallic nanoparticles (BNPs) with varying stoichiometries: (a) In-plane and (b) out-of-plane scattering profiles with modeled fits, showing (c) extracted structural parameters (D, σD/D, H/D, Λ, and w). Ag50Pt50 denotes an equimolar bimetallic nanoparticle composition with a 50:50 atomic ratio of Ag to Pt.

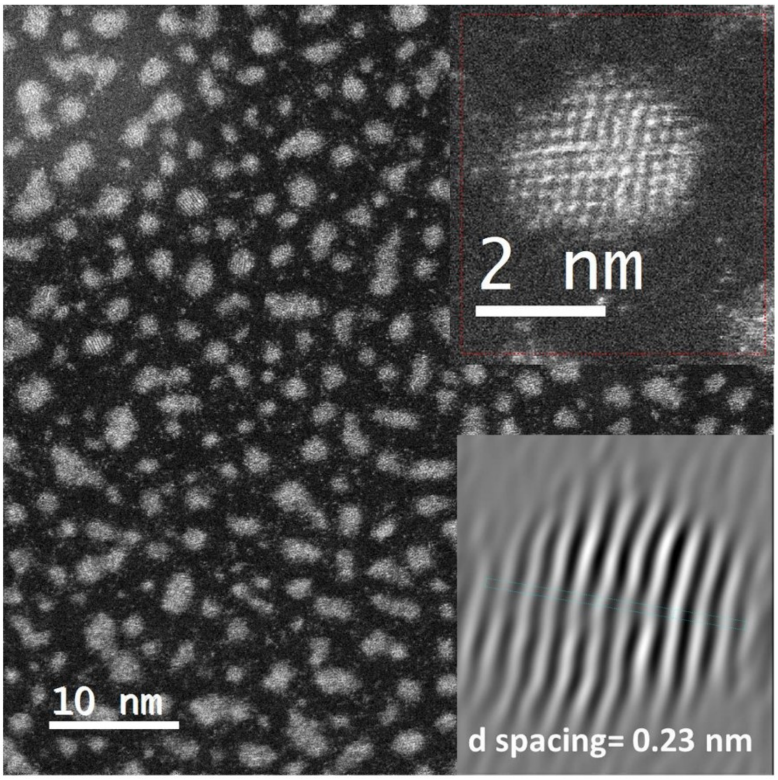

Figure S4: HAADF Image of AgPt alloy nanoparticles on a polymer surface with insets: enlarged view of a selected particle (Top) and its corresponding fast fourier transform (FFT) pattern of the (111) Plane (Bottom).

To assess the uniform distribution and alloying behavior of Ag and Pt in our nanoparticles, we employed high-angle annular dark field (HAADF) imaging **(Figure S4)** to measure the interplanar d-spacing and extract the lattice parameter. The observed d-spacing for AgPt nanoparticles was 0.23 nm, which is close to the (111) plane of the face-centered cubic (fcc) structure. Using this value and the corresponding Miller indices, we calculated a lattice parameter (a) of 0.39 nm. This result aligns well with the theoretical lattice parameter of approximately 0.40 nm predicted by Vegard's law for a 50:50 Ag:Pt alloy composition, indicating ideal mixing and the formation of a solid solution.

Furthermore, the measured d-spacing of 0.23 nm in AgPt falls between those of pure monometallic Ag (0.236 nm) and Pt (0.226 nm) which are predicted by Vegard's law, further supporting the formation of a homogeneous alloy phase rather than phase-segregated or core–shell structures. These findings provide strong evidence for uniform alloying and miscibility in the AgPt system at the nanoscale.

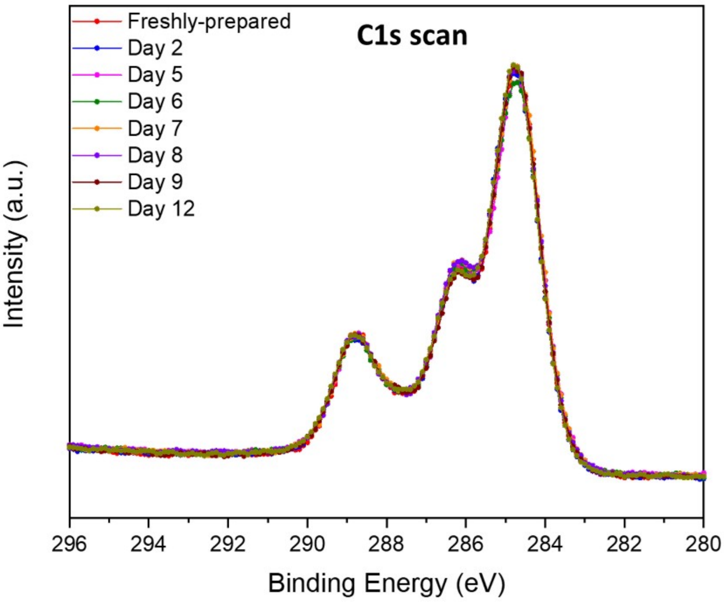

Figure S5: Time-dependent XPS observations showing the evolution of C1s peaks with time.

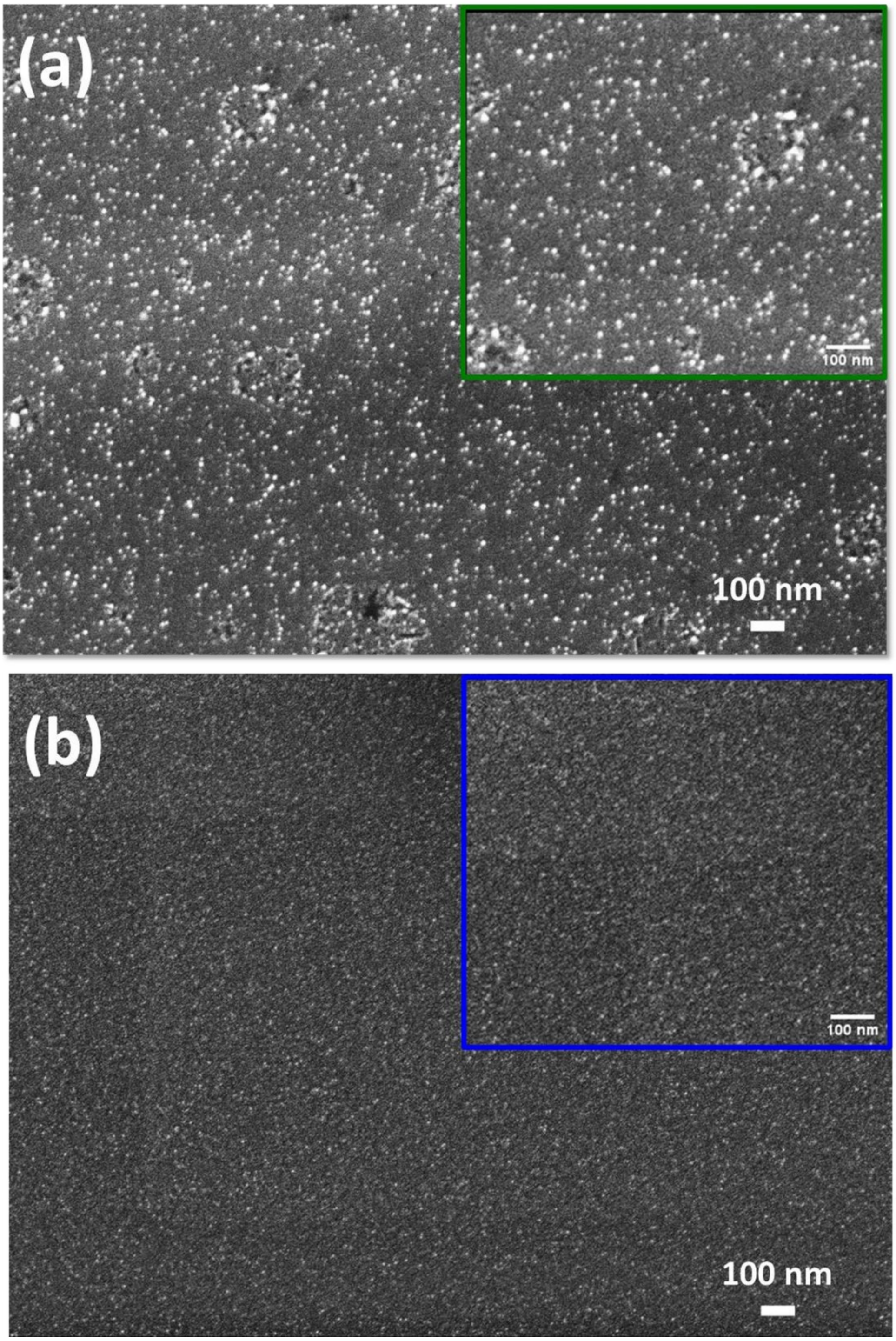

Figure S6: SEM micrographs of bimetallic AgPt nanoalloys after 12 days post-synthesis: (a) deposited on Si/SiO₂ substrates, and (b) deposited on a polymer layer. The insets display magnified views.

Figures S6(a) and (b) reveal a clear distinction in nanoparticle visibility between the polymer and silica matrices, despite equivalent atomic deposition quantities. It is unlikely that such differences would have arisen when the same number of atoms were deposited on both surfaces. A significant portion of NPs appears less visible on the polymer substrate, with notable variations in particle contrast. This suggests that most NPs have become embedded within the polymer layer, instead of remaining on the surface.

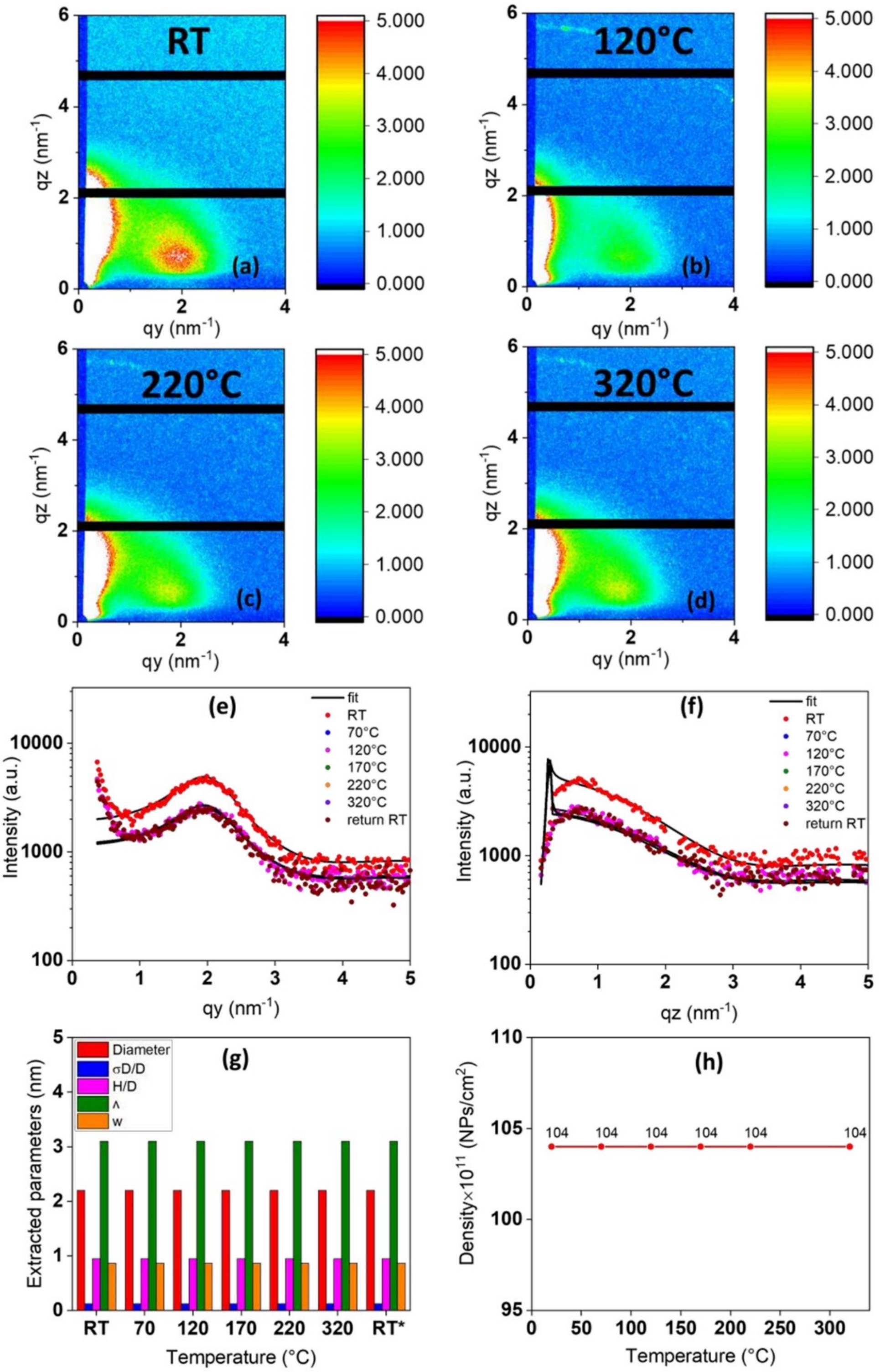

Figure S7: Raw GISAXS 2D patterns of Si/polymer/Pt at different temperatures: (a) RT, (b) 120°C, (c) 220°C and (d) 320°C, scattering intensity profiles with their corresponding fits (e) horizontally and (f) perpendicular to the substrate plane. (g) quantitative analysis of particle characteristics and spatial distribution (diameter, σD/D, H/D, ʌ, and w) from simulated data, and (h) the plot of the density of NPs versus temperature. The scattering intensity profiles exhibit consistent patterns at temperatures of 70°C and 120°C. Similarly, comparable scattering intensity profiles are observed at 170°C, 220°C, 320°C, and upon returning to room temperature. RT* denotes the "Return to Room Temperature" phase after annealing.

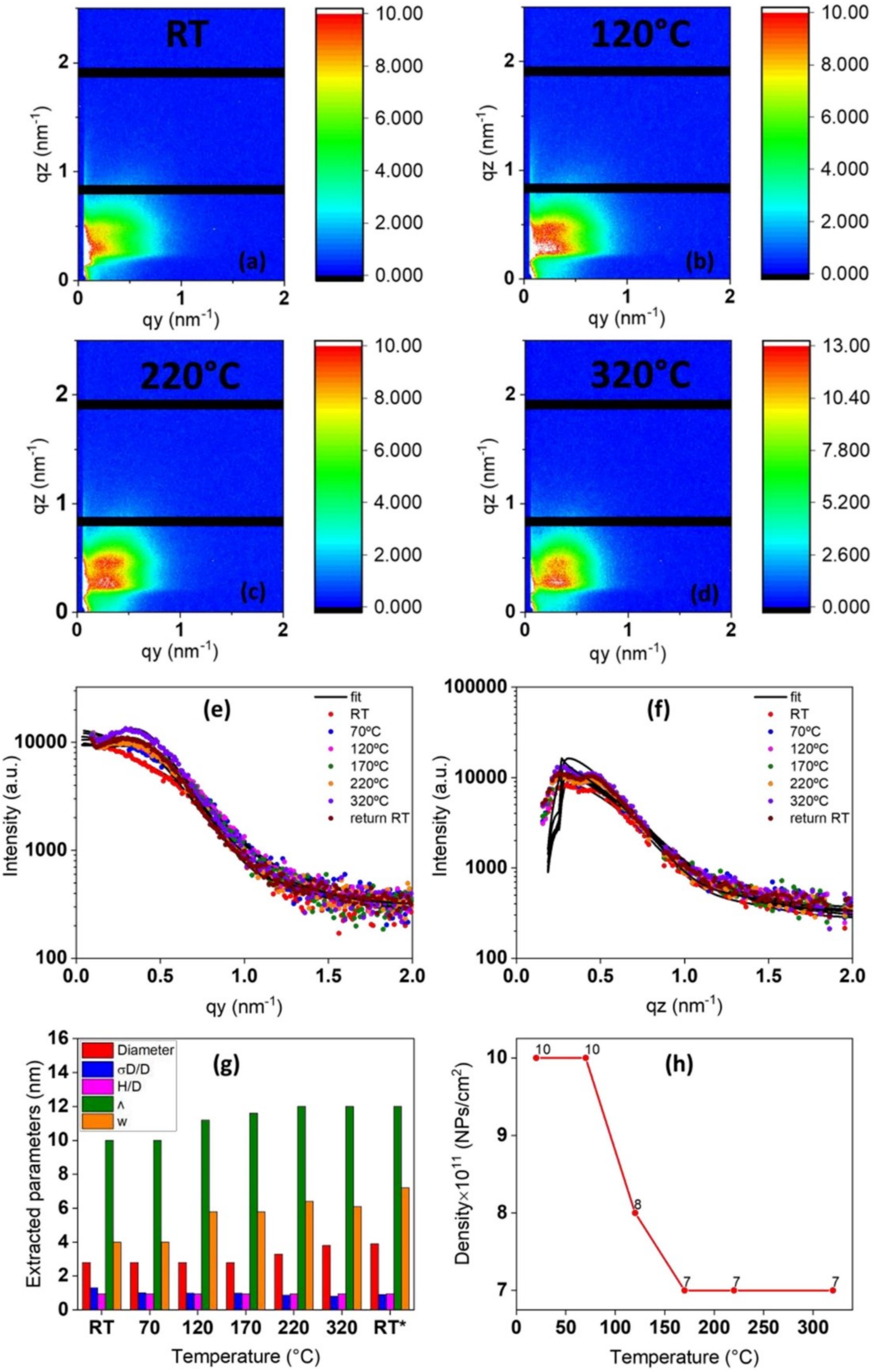

Figure S8: Raw GISAXS 2D patterns of Si/polymer/Ag monometallic at different temperatures: (a) RT, (b) 120°C, (c) 220°C and (d) 320°C, scattering intensity profiles with their corresponding fits (e) horizontally and (f) perpendicular to the substrate plane. (g) quantitative analysis of particle characteristics and spatial distribution (diameter, σD/D, H/D, ʌ, and w) from simulated data, and (h) the plot of the density of NPs versus temperature. RT* denotes the "Return to Room Temperature" phase after annealing.

The incorporation of alloying strategies effectively minimizes polydispersity in both NPs size and interparticle distances throughout the annealing process. This effect is particularly evident when compared to monometallic Ag samples in **Figure S8**, which display larger variations even at the relatively low temperature of 70°C (σD/D = 1.0, w = 4.0). AgPt alloy NPs exhibit superior size uniformity and stability in the polymer matrix, with platinum playing a crucial role in mitigating coalescence, reducing atomic diffusion, and altering nucleation and growth mechanisms. Even at RT, AgNPs exhibit larger sizes (D = 2.8 nm) and greater interparticle distances (ʌ = 10.0 nm) compared to their alloyed counterparts (D = 2.4 nm, ʌ = 3.4 nm). These differences become more pronounced upon annealing, with the diameter of AgNPs increasing to 3.9 nm and interparticle distances extending to 12 nm at 320°C. During GISAXS measurements, a distance of 1380 mm was used with a lower q-range (corresponding to a higher size in the real space) to examine larger structural features of the Ag sample during annealing while also reducing the beam size. The 2D GISAXS patterns of the Ag sample reveal two distinct lobes caused by the collective scattering of all NPs in the illuminated volume, including surface-bound and polymer-confined NPs.

Monometallic PtNPs in **Figure S9** exhibit smaller average diameters and shorter interparticle distances compared to monometallic AgNPs, both at RT and after various stages of annealing. This can be attributed to the lower mobility of Pt atoms and PtNPs, as discussed earlier. Unlike AgNPs and AgPt alloys, monometallic PtNPs undergo no temperature-dependent structural evolution. A distinct thermal hierarchy is evident among the NPs systems. PtNPs attain equilibrium at RT without requiring annealing, whereas AgNPs demonstrate susceptibility to thermal alterations, with changes persisting even after cooling to RT. In contrast, AgPt alloy nanoparticles necessitate heating to 320°C to achieve structural stabilization. This hierarchy underscores the varying thermal stabilities and equilibration requirements across the different nanoparticle compositions.

Experimental Part

Characterizations

Grazing Incidence Small Angle X-ray Scattering measurements and simulations: GISAXS measurements were performed using a SAXS/GISAXS Xeuss 1.0 system equipped with a Microfocus GeniX-3D Cu X-ray source (Ultra Low Divergence, λ = 1.5418 Å). The source provided a total photon flux of approximately 10^6 ph/s at the sample, with a brightness in the range of 10^7 photons/s/mm^2/mrad^2. Experiments were conducted in high-resolution mode at an incident angle (α_i) of 0.22° close to the total reflection angle that maximize the intensity available for scattering and reduce the analysis depth to the over-layer. Scattering patterns, characterized by two symmetrical intensity lobes, were collected using a Dectris Pilatus 3R 300K detector positioned at a sample-to-detector distance of 570 mm. Quantitative analysis involved extracting one-dimensional data through two specific cuts: a qy cut parallel to the substrate plane near the Yoneda peak and a qz cut perpendicular to the substrate through the lobe center [3–5]. The scattered intensity profiles along both qy and qz were simultaneously fitted using IsGISAXS software [6], which incorporates the Distorted Wave Born Approximation (DWBA) and Local Monodisperse Approximation (LMA). This analysis yielded key structural parameters of the BNPs-loaded polymer system, including nanoparticle diameter (D), height-to-diameter aspect ratio (H/D), inter-particle spacing (ʌ), size and gap distribution parameters (σD/D and w), and nanoparticle density (ρ).

X-ray Photoelectron Spectroscopy (XPS): Measurements were taken using a Thermoscientific Escalab Xi$^+$ spectrometer connected directly into the UHV molecular beam deposition system. This configuration enables in-situ, real-time surface analysis without breaking the vacuum or exposing samples to atmospheric conditions. It incorporates a dual charge compensation mechanism utilizing low-energy electrons and Ar ions, alongside two distinct X-ray sources: a monochromatic Al Kα (1486.6 eV) and a higher-energy Ag Lα (2984.2 eV), enabling comprehensive surface analysis across varied sample types and energy ranges. Monochromaticity and detection performance allow a kinetic energy resolution of less than 0.1 eV. The instrument offers adjustable standard spot sizes ranging from 200 to 900 µm, with high-resolution capability down to ~20 µm. Photoelectrons were collected normally to the sample surface (θ = 90° between the analyzer and sample surface), providing an analysis depth of approximately 10 nm in polymer matrix. Data acquisition and processing were performed using Avantage software, enabling quantitative determination of elemental compositions and chemical states.

Microscopic techniques: TEM imaging was conducted using a PHILIPS CM20 conventional microscope, operating at an accelerating voltage of 200 kV and a resolution of 0.14 nm. Sample preparation involved depositing the polymer layer on the carbon-coated side of TEM grids, ensuring a thickness below 100 nm to have an ideal interaction with the electron beam. These polymer-coated TEM grids were later introduced into the MBE chamber for NPs deposition to quantify their structural characteristics. The JEOL IT800SHL microscope was employed to capture high-resolution SEM images with an accelerating voltage of 1 kV and a working distance of 2 mm. Surface topography was characterized using a non-contact Zygo NewView 7100 interferometric profilometer for a precise quantification of surface roughness and thickness of polymer layer.

Optical techniques: Polarization-dependent optical characterization was conducted using a WOOLAM M2000X ellipsometry. The instrument measured the amplitude ratio (Ψ) and phase difference (Δ) between p- and s-polarized light reflected from the sample surface. Subsequent data analysis required constructing an optical model using CompleteEase software to extract physical parameters such as optical constants, absorption coefficients, and film thicknesses from the measured Ψ and Δ values.

Measurements were performed over a broad spectral range of 245-1000 nm, with an incident angle of 70° chosen to maximize measurement sensitivity. The probing light beam had a typical spot size of 2-5 mm. A Thermo Fisher Scientific Evolution E200 UV-Vis spectrophotometer was used to examine the optical properties of the samples. This instrument operates in reflectance mode, directly measuring absorbance across a broad spectral range of 190-1100 nm. The system incorporates a 60 mm diameter integrating sphere to ensure uniform light collection and improved intensity homogenization. The spectrophotometer offers high spectral resolution, with a wavelength bandwidth of 1 nm. All spectra were baseline-corrected using an integrating sphere.

Infrared Fourier Transform (FT-IR): Analysis was performed using a JASCO 6600 spectrophotometer. The instrument was coupled with a Hamamatsu Lightningcure LC8 UV lamp via a fiber-optic cable to facilitate the study of photopolymerization process. This UV source, functioning at a central wavelength of 365 nm and delivering an intensity of 180 mW/cm², enabled in-situ monitoring of UV-induced reactions, allowing real-time observation of chemical changes during photopolymerization (chemical state and conversion rate). Experimental constraints in the FT-IR setup, particularly the fixed lamp-to-sample distance, required the use of a light intensity different from that used in the polymer's photo-induced synthesis (360 mW/cm²).

References

1. Balan L, Burget D. Synthesis of metal/polymer nanocomposite by UV-radiation curing. European Polymer Journal. 2006;42(12):3180–9.

2. Balan L, Malval JP, Lougnot DJ. In situ photochemically assisted synthesis of silver nanoparticles in polymer matrixes. Silver nanoparticles. 2010;79–92.

3. Andreazza P. Probing Nanoalloy Structure and Morphology by X-Ray Scattering Methods. In: Alloyeau D, Mottet C, Ricolleau C, editors. Nanoalloys [Internet]. London: Springer London; 2012 [cited 2025 Jan 7]. p. 69–112. (Engineering Materials). Available from: https://link.springer.com/10.1007/978-1-4471-4014-6_3

4. Andreazza P, Mottet C, Andreazza-Vignolle C, Penuelas J, Tolentino HCN, De Santis M, et al. Probing nanoscale structural and order/disorder phase transitions of supported Co-Pt clusters under annealing. Phys Rev B. 2010 Oct 28;82(15):155453.

5. Renaud G, Lazzari R, Leroy F. Probing surface and interface morphology with grazing incidence small angle X-ray scattering. Surface Science Reports. 2009;64(8):255–380.

6. Lazzari R. IsGISAXS: a program for grazing-incidence small-angle X-ray scattering analysis of supported islands. Journal of Applied Crystallography. 2002;35(4):406–21.